

ARMY RESEARCH LABORATORY



Dynamic Behavior of Polycrystalline Tantalum

by Scott E. Schoenfeld

ARL-TR-1560

December 1997

DTIC QUALITY INSPECTED 4

19980318 075

Approved for public release; distribution is unlimited.

The findings in this report are not to be construed as an official Department of the Army position unless so designated by other authorized documents.

Citation of manufacturer's or trade names does not constitute an official endorsement or approval of the use thereof.

Destroy this report when it is no longer needed. Do not return it to the originator.

Army Research Laboratory

Aberdeen Proving Ground, MD 21005-5066

ARL-TR-1560

December 1997

Dynamic Behavior of Polycrystalline Tantalum

Scott E. Schoenfeld

Weapons and Materials Research Directorate, ARL

Abstract

A description for the strain-rate and temperature-dependent behavior of pure tantalum (Ta) at large strains is developed. An integral part of the model incorporates the kinematics of crystallographic slip, and thus, the rotation of single crystals within the material, so as to reflect the evolution of anisotropy resulting from applied mechanical deformation. Such deformation is accommodated via bulk dislocation motion and governed by interactions that may or may not be thermally assisted. The model represents each discrete slip system as a single facet in a multisurface plasticity theory, which is well suited to high-rate numerical methods (explicit integration schemes). A formulation of this type allows for the complete kinematic decomposition of macroscopic material rotations and the rotations of single crystals due to motion through the lattice. Applications to high-rate deformation in polycrystals is conducted within a finite element implementation by invoking a Taylor criterion for interaction between the macroscopic and the mesoscopic (single-crystal) length scales. The model behavior is examined in application to high-rate problems with increasingly complex geometries (homogeneous uniaxial compression, the impact of a textured cylindrical bar into a rigid anvil, and the explosive deep-drawing of a Ta disk). The final example compares through-thickness deformation in the Ta disk as a function of initial texture and, therefore, emphasizes the profound effects of plastic anisotropy during finite deformation.

Acknowledgments

The author would like to acknowledge financial support from the U.S. Army Research Laboratory (ARL), Weapons and Materials Research Directorate. In particular I would like to thank Drs. Andrew Dietrich and Thomas Wright of ARL for their invaluable encouragement and Mr. Eric Edwards of LB&B Associates for his careful review of this manuscript.

INTENTIONALLY LEFT BLANK

Table of Contents

| | <u>Page</u> |
|---|-------------|
| List of Figures | vii |
| 1. Introduction | 1 |
| 2. Material Description for Crystallographic Slip | 3 |
| 2.1 Description for Thermally Activated Dislocation Glide | 3 |
| 2.2 Single-Crystal Kinematics | 5 |
| 3. Numerical Implementation | 7 |
| 3.1 Single-Crystal Return Algorithm | 7 |
| 3.2 Length-Scale Interaction | 10 |
| 4. Application to Dynamic Deformation in Pure Ta | 13 |
| 4.1 Uniaxial Compression | 13 |
| 4.2 Taylor Impact Cylinder | 14 |
| 4.3 Explosive Deep-Drawing | 16 |
| 5. Discussion | 23 |
| 6. References | 25 |
| Distribution List | 29 |
| Report Documentation Page | 33 |

INTENTIONALLY LEFT BLANK

List of Figures

| <u>Figure</u> | <u>Page</u> |
|---|-------------|
| 1. Six facets composing the 2D plane strain yield surface for the $\{110\} < 111 >$ slip family in a single crystal aligned with the macroscopic axes of stress . . | 11 |
| 2. Enlarged view of two yield facets from Figure 1 showing an anomaly in the algorithm and the correct returned position | 12 |
| 3. $\{100\}$, $\{110\}$, and $\{111\}$ pole figures for Ta compressed uniaxially to a true strain of 1.0 | 14 |
| 4. Evolution history of the $\{100\}$, $\{110\}$, and $\{111\}$ pole figures at the center of the impacted surface during the Taylor-cylinder impact experiment. Pole figures are shown along the impact direction; this direction was previously the transverse direction in the rolled Ta sheet material | 15 |
| 5. Two views along the impact direction of the Taylor cylinder; (a) contours of effective plastic strain in the ovalized footprint, and (b) the ovalized footprint relative to the initially circular cross section which is retained away from the impact surface | 16 |
| 6. The explosive deep-drawing process; an initial finite element mesh (bottom) depicting a Ta disk and high-explosive charge. Initiation of the explosive imparts both an upward velocity to the disk and deformation into a cup-like configuration. Effective strain contours in the explosively deep-drawn disk at 50 μs are shown at the top of the figure | 18 |
| 7. Texture evolution during explosive deep-drawing. Columns show the $\{100\}$, $\{110\}$, and $\{111\}$ pole figures. The top row characterizes the initially random distribution of grains that is homogeneous throughout the disk. By 50 μs , there is a gradient in texture from the nose (center row) extending radially outward in the deep-drawn cup. Texture in the high-strain tail region is shown in the bottom row | 19 |
| 8. $\{111\}$ pole figures showing texture evolution due to three different ideal fiber textures. The initial homogeneous textures (first column) correspond to ideal $\{100\}$, $\{110\}$, and $\{111\}$ fiber textures. The second column shows final deformation textures in the nose region while the third column shows final texture in the high-strain tail region | 21 |
| 9. Contours of deviatoric through-thickness stress (units are in pascals) plotted on the deformed configuration of the explosively formed material at 3 μs . . | 22 |
| 10. Effective strain contours on the deformed configuration for explosive deep-drawn material at 50 μs . The initial textures were distributed homogeneously in the disk and then allowed to evolve with deformation. | 24 |

11. A comparison of effective strain contours over the deformed shapes from the initially random-oriented material and the material with an initial $\{111\}$ fiber texture. The two calculations are shown on opposite sides of the plane of symmetry for the calculation 25

1. Introduction

By its very nature, crystallographic glide on a restricted set of slip directions produces anisotropic plastic behavior in the single-crystal constituents of a polycrystalline aggregate. Even though a random-oriented polycrystal may exhibit isotropic mechanical properties, finite deformation in polycrystalline aggregates is often accompanied by severe reorganization of the material's microstructure. Upon such reorganization, initially random distributions of single-crystal constituents may begin to align in preferred orientations (texture). Therefore, within materials that deform by crystallographic slip, dislocation motion causes grain rotations and, thus, after large deformation, may cause severe mechanical anisotropy even in materials that are initially isotropic.

Such large strains may arise within certain general engineering applications, but more often they may arise during the thermo-mechanical processing of stock material used in the production of engineering systems. In the latter case, analysis of these systems may be critically dependent on knowledge of the initial material state and inherent material anisotropy. For example, the construction of vehicle body panels from rolled sheet involves a material with an initially high degree of anisotropy due to the previous rolling procedure. An analysis of such a structure may have to account for initial anisotropy, but the evolution of anisotropy during the life of the structure would not be great. High-strain-rate applications, however, often involve large deformation of material that has already undergone extreme microstructural reorientations during the initial processing (i.e., manufacturing process) and now faces further large deformation, microstructural evolution, and, thus, evolving anisotropy during its performance lifetime. More importantly, evolving anisotropy may be critically important in setting the stage for late-strain localization and ultimate structural failure. Accurate analysis of such devices depends on understanding how material anisotropy evolves during the deformation of complex geometries and how such anisotropies affect the dynamic evolution of macroscopic features.

Macroscopic mechanical anisotropy evolves with increasing deformation via a number of mechanisms. In brittle materials, changes in the preferred deformation behavior is usually a function of damage on either the micro or macro scale. In ductile metals, such as Ta, directional dependence evolves via several mechanisms that commonly involve the motion of dislocations through the crystallographic lattice of single crystals, and in polycrystalline materials, the interaction and reorientation of these crystals.

Observations of macroscopic phenomenology during the deformation of anisotropic materials have led to the formulation of anisotropic yield surfaces [1, 2] and kinematic hardening models [3] that are capable of reflecting the macroscopic directionality of such materials. These models, however, are only a *description* of observations and, even when well calibrated, will never become predictive at large deformation when the initial anisotropy begins to evolve. Within this framework, Maudlin et al. [4, 5] have sought to incorporate the crystallographic orientations into an anisotropy model by direct measurement using x-ray diffraction. These measured orientations are then used to formulate a faceted yield surface as a convex flow envelope representing the initial grain orientations in the material. Although ideally suited for high-rate applications and physically based, this yield description lacks evolution of grain orientations at large strains.

Physically based models for texture evolution have been under development for a number of years [6, 7] but have only recently been applied to deformation at high strain rates [8, 9]. Applications of these models have mainly been concerned with the analysis of homogeneous deformations. Robust polycrystal implementations for the analysis of nonhomogeneous deformation fields are indeed quite new [10, 11]. Most recently, Kothari et al. [12] have described an elasto-viscoplastic constitutive model for polycrystalline Ta deforming at high strain rates. This model has been implemented into the finite element code ABAQUS [13] and used to analyze the impact of a pretextured Ta rod.

Appropriately, this work is concerned with describing how Ta and other ductile polycrystals behave when deforming to large strains at high rates. We begin with a description of the fundamental kinematics of crystallographic slip in single crystals, incorporating a likely constitutive description for the elasto-viscoplastic behavior of single crystals and an appropriate numerical implementation of the combined constitutive theory. This single-crystal behavior is used in an appropriate averaging technique to achieve a description for polycrystalline material behavior that reflects the evolution of material anisotropy via the underlying physical mechanisms. This model is especially suited for implementation into a coupled thermomechanical, large-strain, high-rate finite element formulation for solving complex boundary value problems. Example calculations include both homogeneous and nonhomogeneous uniaxial compression of random and pretextured Ta stock. The model is then used to investigate through-thickness sheet thinning during explosive deep-drawing, a dramatic example of texture-induced plastic-anisotropy with practical implications.

Notation used in this work is based on the following convention. Scalars are denoted by mathematical italics, (A , a , α), vectors by lowercase boldface (\mathbf{a}), second-order tensors by uppercase boldface (\mathbf{A}), and fourth-order tensors by calligraphic uppercase boldface (\mathcal{K}). The summation convention is used for Latin indices. Superscripts pertaining to slip systems are written in Greek letters; summation over these are indicated explicitly. Dot and double dots are used to indicate the following products:

$$\mathbf{F} \cdot \mathbf{m} \rightleftharpoons F_{ij}m_j, \quad \mathbf{C} : \mathbf{C} \rightleftharpoons C_{ij}C_{ji};$$

and

$$\mathcal{K} : \mathbf{L} \rightleftharpoons \mathcal{K}_{ijkl}L_{lk}; \quad \boldsymbol{\tau} \cdot \mathbf{D} \rightleftharpoons \tau_{ik}D_{kj}.$$

Finally, time derivatives are denoted by superposed dots, e.g.:

$$\dot{\mathbf{F}} = \partial \mathbf{F} / \partial t,$$

while the transpose of a tensor is designated by the superscript T .

2. Material Description for Crystallographic Slip

The following section, beginning with a description for the thermally activated glide of dislocations along a restricted set of slip directions and plane normals followed by the kinematic implications of restricted glide, constitutes the current model for thermo-mechanical deformation in a single crystal.

2.1 Description for Thermally Activated Dislocation Glide

A framework for the bulk motion of dislocation glide that is both temperature and strain rate dependent [14, 15] has been successfully calibrated to Ta and Ta-W alloys under a broad range of temperatures and strain rates [16]. Most recently, Kothari and Anand [12] incorporated a similar model to explicitly describe crystallographic slip on discrete slip systems and slip planes. The following section is a brief review of how dislocations may interact with various obstacles, and, how these obstacles may be affected by changes in temperature and strain rate.

Dislocation motion is assumed to result from both applied stress and statistical fluctuations due to thermal vibrations. The motion is affected by obstacles, both long and

short range with respect to lattice dimensions; long range obstacles typically include grain boundaries or large, second-phase particles while the short range barriers may include forest dislocations, interstitial or solute atoms, small precipitates, or in the case of pure Ta, large Peierls stresses [16, 17, 18]. Such obstacles are said to characterize the material “state,” or, in terms of stress, where τ^α is the resistance to dislocation motion on the α system, we say

$$\tau^\alpha = \tau_a^\alpha + \sum_{i=1}^r S_i(\theta, |\dot{\gamma}^\alpha|) \tau_i^\alpha, \quad (1)$$

where τ_a^α is the resistance associated with long-range interactions that cannot be thermally assisted. Each type of thermally activated obstacle (summed over i) that may resist dislocation motion is characterized by τ_i^α , the stress required to overcome the barrier, or constant “structure,” at 0 K. The temperature and strain-rate contributions to overcoming such barriers are reflected in the $S_i(\theta, |\dot{\gamma}^\alpha|)$ terms, where θ denotes temperature and $\dot{\gamma}^\alpha$ denotes the slip rate on the α 'th slip plane. Since τ_i^α defines the maximum barrier for a given structure, the S_i are by definition ≤ 1 . In the previous equation, thermally activated obstacles are considered on the scale of the crystallographic lattice dimensions; obstacles such as the Peierls resistance to glide may be overcome by thermal activation energy alone. Thus, the functions $S_i(\theta, |\dot{\gamma}^\alpha|)$ lower the resistance due to the material state τ_i^α by accounting for the statistical frequency that such obstacles may be overcome by thermal fluctuations. Each $S_i(\theta, |\dot{\gamma}^\alpha|)$ describes the short-range interaction kinetics via the phenomenological [15] form

$$S(\theta, |\dot{\gamma}^\alpha|)_i = \left[1 - \left(\frac{k\theta \ln(\frac{\dot{\gamma}_{0,i}}{|\dot{\gamma}^\alpha|})}{\mu b^3 g_{0,i}} \right)^{\frac{1}{q_i}} \right]^{\frac{1}{p_i}}, \quad (2)$$

where b is the lattice Burgers vector, $g_{0,i}$ is the normalized activation energy for dislocation/obstacle interaction, p_i and q_i are factors that represent geometry of i^{th} obstacle type, and $\dot{\gamma}_{0,i}$ is a reference shear rate taken to be the same on all slip systems [12]. The dislocation kinetics of such flow is discussed in detail in other works [14, 15, 19].

Kothari and Anand [12], when considering pure Ta, allow only a single thermally assisted obstacle (representing the Peierls barrier), and allow only the athermal structure to evolve with dislocation motion.

In order to model deformation behavior in pure Ta over a broad range of temperatures and strain rates, Chen and Gray [16] distinguish between the thermally activated Peierls barrier and structure associated with dislocation hardening and recovery (dislocation accumulation and annihilation). Further, they differ from Kothari and Anand [12] by assuming

that this second mechanism is thermally activated. Following Chen and Gray [16], equation (1) becomes

$$\tau^\alpha = \tau_a^\alpha + S_p \tau_p^\alpha + S_\gamma \tau_\gamma^\alpha, \quad (3)$$

where S_p and τ_p^α are associated with the Peierls stresses and do not evolve during deformation. The S_γ and τ_γ^α pair are associated with dislocation density. S_γ will take the form of equation (2), and τ_γ^α will evolve according to the Peirce et al. [20] structure that has been applied within this framework by Kothari and Anand [12], i.e.,

$$\dot{\tau}_\gamma^\alpha = \sum_\beta h^{\alpha\beta} |\dot{\gamma}^\beta|. \quad (4)$$

The hardening moduli, $h^{\alpha\beta}$, is given as

$$h^{\alpha\beta} = [q + (1 - q)\delta^{\alpha\beta}] h^\beta, \quad (5)$$

where h^β denotes the self-hardening rate and q denotes the ratio of self versus latent hardening. As in Chen and Gray [16], the self-hardening due to dislocation motion will be assigned the form proposed by Follansbee and Kocks [15]

$$h^\beta = h_0^\beta \left\{ 1 - \frac{\tanh \left[\zeta \frac{\tau_\gamma^\alpha}{\tau_{\gamma s}^\alpha} \right]}{\tanh [\zeta]} \right\}, \quad (6)$$

where $\tau_{\gamma s}^\alpha$ takes the rate- and temperature-dependent form

$$\tau_{\gamma s}^\alpha = \tau_{\gamma s 0}^\alpha \left(\frac{\sum |\dot{\gamma}^\beta|}{\dot{\gamma}_0^\alpha} \right)^{\frac{k\theta}{\mu b^3 A}}. \quad (7)$$

In the previous two equations, ζ and $\tau_{\gamma s 0}^\alpha$ are material constants, b is the magnitude of the Burgers vector, k is the Boltzmann constant, and $\dot{\gamma}_0^\alpha$ is a reference rate of shearing.

2.2 Single-Crystal Kinematics

The motion of an elasto-plastic single crystal can be partitioned as the result of elastic stretching accompanied by rigid-body rotation and simple shearing along the various slip systems of the crystal. The shearing motion is due to dislocation movement along the slip systems but is described in a bulk continuum framework. The motion of the single crystal then can be decomposed into a plastic part, due to crystallographic glide, and an elastic

part, due to lattice stretching and rotation. Using \mathbf{F} to designate the deformation gradient of the single crystal, a multiplicative decomposition [21] is written in component form as

$$\mathbf{F} = \mathbf{F}^* \cdot \mathbf{F}^p, \quad (8)$$

where \mathbf{F}^p is due to the net motion of dislocations and \mathbf{F}^* contains the elastic distortion and rigid-body rotation of the lattice [22, 23, 24]. The slip direction of a particular system, α , is denoted by $\mathbf{s}^{(\alpha)}$ and must lie in the slip plane with normal $\mathbf{m}^{(\alpha)}$. The orthonormal pair $\mathbf{s}^{(\alpha)}$ and $\mathbf{m}^{(\alpha)}$ convect with the lattice to become

$$\mathbf{s}^{*(\alpha)} = \mathbf{F}^* \cdot \mathbf{s}^{(\alpha)} \quad (9)$$

and

$$\mathbf{m}^{*(\alpha)} = \mathbf{m}^{(\alpha)} \cdot \mathbf{F}^{*-1}. \quad (10)$$

The total velocity gradient, \mathbf{L} , can then be written in an additive decomposition, i.e.,

$$\mathbf{L} = \dot{\mathbf{F}} \cdot \mathbf{F}^{-1} = \mathbf{L}^* + \mathbf{L}^p, \quad (11)$$

with \mathbf{L}^* and \mathbf{L}^p representing the elastic and plastic parts, respectively. The inelastic deformation due to crystallographic slip is the linear summation of slip along some active subset of the total number of restricted glide systems. If we denote M_{act} to be this subset, then

$$\mathbf{L}^p = \sum_{\alpha}^{M_{act}} \mathbf{s}^{*(\alpha)} \otimes \mathbf{m}^{*(\alpha)} \dot{\gamma}^{(\alpha)} = \sum_{\alpha}^{M_{act}} \mathbf{P}^{\alpha} \dot{\gamma}^{(\alpha)}. \quad (12)$$

The plastic part of the velocity gradient can be further decomposed into the symmetric rate of stretching, \mathbf{D}^p , and the antisymmetric plastic spin, $\mathbf{\Omega}^p$,

$$\mathbf{L}^p = \mathbf{D}^p + \mathbf{\Omega}^p. \quad (13)$$

We denote the symmetric and antisymmetric parts of the Schmid tensor, \mathbf{P}^{α} , by \mathbf{R}^{α} and \mathbf{W}^{α} , respectively, and write

$$\mathbf{R}^{(\alpha)} = \frac{1}{2} [\mathbf{s}^{*(\alpha)} \mathbf{m}^{*(\alpha)} + \mathbf{m}^{*(\alpha)} \mathbf{s}^{*(\alpha)}] \quad (14)$$

and

$$\mathbf{W}^{(\alpha)} = \frac{1}{2} [\mathbf{s}^{*(\alpha)} \mathbf{m}^{*(\alpha)} - \mathbf{m}^{*(\alpha)} \mathbf{s}^{*(\alpha)}] \quad (15)$$

so that

$$\mathbf{D}^p = \sum_{\alpha}^{M_{act}} \mathbf{R}^{(\alpha)} \dot{\gamma}^{(\alpha)} \quad (16)$$

and

$$\mathbf{\Omega}^p = \sum_{\alpha}^{M_{act}} \mathbf{W}^{(\alpha)} \dot{\gamma}^{(\alpha)} . \quad (17)$$

During deformation, any crystallographic axis, (e.g., the \mathbf{c} axis) will rotate with the lattice spin, $\mathbf{\Omega}$ as

$$\dot{\mathbf{c}} = \mathbf{\Omega}^* \cdot \mathbf{c}, \quad (18)$$

where $\mathbf{\Omega}^*$ is the difference between the total spin, $\mathbf{\Omega}$, and the previously defined plastic spin, i.e.,

$$\mathbf{\Omega}^* = \mathbf{\Omega} - \mathbf{\Omega}^p . \quad (19)$$

3. Numerical Implementation

Finite element formulations for the analysis of wave propagation and dynamic inertial effects typically implement the equations of motion in an explicit formulation where time steps are limited to some fraction of the Courant stability limit. As such, it is common practice to assume constant strain rates (as calculated from the previous time step) across the time step and implement rate-dependent material behavior as step-wise rate independent [25]. Stress rotations are updated at half-time increments on either side of the constitutive update, thus creating an objective stress update decoupled from the constitutive calculation.

3.1 Single-Crystal Return Algorithm

Denoting $\boldsymbol{\sigma}$ as the rotated, deviatoric Cauchy stress, the resolved shear stress on any particular glide system, denoted by α , is given as

$$\tau^{\alpha} = \mathbf{P}^{\alpha} : \boldsymbol{\sigma} . \quad (20)$$

Assuming that slip occurs when the resolved shear stress reaches some threshold value, $\tau^{\alpha} = \tau_c^{\alpha}$, we can use the previous equation to define a yield function, f^{α} , for the α^{th} slip system as

$$f^{\alpha} \equiv |\boldsymbol{\sigma} : \mathbf{P}^{\alpha}| - \tau_c^{\alpha} = 0, \quad (21)$$

where the components of \mathbf{P}^{α} are the previously defined direction cosines that resolve $\boldsymbol{\sigma}$ into the direction of slip. Note here that for the purposes of a numerical algorithm, if $\tau^{\alpha} \leq -\tau_c^{\alpha}$ (i.e., the resolved shear stress exceeds the critically resolved shear stress so as to create slip

in the $-\mathbf{s}^{*(\alpha)}$ direction), then the slip vector, $\mathbf{s}^{*(\alpha)}$, is temporarily changed to $-\mathbf{s}^{*(\alpha)}$ so that only positive $\dot{\gamma}$'s will be considered.

The collection of linear yield functions described by equation (21) resembles a Tresca-type yield condition that was actually described for single crystals by Koiter [26]. Simo, Kennedy, and Govindjee [27] described a full plasticity theory for a collection of smooth, multifaceted yield surfaces. The following is an application of the rate-independent Simo, Kennedy, and Govindjee [27] theory applied to the Koiter [26] yield conditions and the single-crystal kinematics described previously.

Begin with a trial elastic update of the stress using a generalized form of Hooke's Law,

$$\boldsymbol{\sigma}^{tr} = \boldsymbol{\sigma}^{old} + \mathcal{L} : \mathbf{L}\Delta t, \quad (22)$$

where \mathcal{L} is the material elastic moduli and Δt is the integration time step size. The calculated $\boldsymbol{\sigma}$ is then used to evaluate f^α for each slip system. If no facets are violated (i.e., $f^\alpha \leq 0$ for all α) then $\boldsymbol{\sigma}^{tr}$ is accepted as the current stress state, $\dot{\gamma}^\alpha = 0$ for all α , and the calculation continues. If the trial stress state causes any $f^\alpha > 0$, then that facet is added to a list of potentially active slip systems. The discussion that follows will be applied to the set of M_{act} *potentially* active yield facets.

The total plastic flow results from the linear sum of plastic flow along each planar facet. Applying the flow rule in this manner over the M_{act} smooth facets recovers equation (12) as

$$\mathbf{L}^p = \sum_{\beta=1}^{M_{act}} \dot{\lambda}^\beta \frac{\partial f^\beta}{\partial \boldsymbol{\sigma}} = \sum_{\beta=1}^{M_{act}} \dot{\lambda}^\beta \mathbf{P}^\beta. \quad (23)$$

It is important to note here that the scalar multipliers, $\dot{\lambda}^\beta$, in the plasticity theory become exactly the slip rates, $\dot{\gamma}^\beta$, from the single-crystal theory. This allows for the complete solution of the coupled single-crystal/multifaceted flow theory.

Assuming that τ^α remains constant over the time step, then the stress rate is given by

$$\dot{\boldsymbol{\sigma}} = \mathcal{L} : \mathbf{L}^* = \mathcal{L} : \{\mathbf{L} - \mathbf{L}^p\} \quad (24)$$

and the condition for plastic consistency is met by

$$\dot{f}^\alpha = \frac{\partial f^\alpha}{\partial \boldsymbol{\sigma}} : \dot{\boldsymbol{\sigma}} = 0. \quad (25)$$

Substitution of (21), (24), and (23) into the previous equation gives an M_{act} by M_{act} system of equations for the slip rates as

$$\mathbf{P}^\alpha : \mathcal{L} : \mathbf{L} - \sum_{\beta=1}^{M_{act}} \mathbf{P}^\alpha : \mathcal{L} : \mathbf{P}^\beta \dot{\gamma}^\beta = 0 \quad (26)$$

for $\alpha = 1$ to M_{act} . As discussed previously, the set of M_{act} systems is considered to be only potentially active. It is actually the condition $\dot{\gamma}^\beta > 0$ (not $f^\beta > 0$) that activates the β^{th} slip system. Therefore, each calculated $\dot{\gamma}^\beta$ must be checked for activation. If $\dot{\gamma}^\beta \leq 0$, then that system is dropped from the list of potentially active systems and equation(26) is reconstructed for the $M_{act}-1$ slip systems. The process is repeated until all $\dot{\gamma}^\beta > 0$.

Once the slip rates are known, the stress state can be relaxed back onto the yield surface as

$$\boldsymbol{\sigma} = \boldsymbol{\sigma}^{tr} - \sum_{\beta=1}^{M_{act}} \mathcal{L} : \mathbf{P}^\beta \dot{\gamma}^\beta \Delta t, \quad (27)$$

and the grain rotation can be updated consistent with the single-crystal kinematics. If we denote $\boldsymbol{\Phi}$ as the the lattice orientation of a particular grain with respect to the lab axis, then the lattice spin is determined by $\boldsymbol{\Omega}^*$ as per Asaro and Rice [28].

$$\boldsymbol{\Phi}(t + \Delta t) = \tilde{\boldsymbol{\Phi}} \cdot \boldsymbol{\Phi}(t), \quad (28)$$

where

$$\tilde{\boldsymbol{\Phi}} = \exp(\boldsymbol{\Omega}^* \Delta t). \quad (29)$$

We employ the Cayley-Hamilton theorem in order to expand $\exp(\hat{\boldsymbol{\Omega}})$ with $\hat{\boldsymbol{\Omega}} = \boldsymbol{\Omega}^* \Delta t$ as

$$\exp(\hat{\boldsymbol{\Omega}}) = \mathbf{I} + \frac{\sin(w)}{w} \hat{\boldsymbol{\Omega}} + \frac{1 - \cos(w)}{w^2} \hat{\boldsymbol{\Omega}}^2 \quad (30)$$

and $w^2 = \hat{\Omega}_{23}^2 + \hat{\Omega}_{13}^2 + \hat{\Omega}_{12}^2$.

As an illustrative example, consider the $\{110\} < 111 >$ family of slip systems (later, both $\{110\} < 111 >$ and $\{112\} < 111 >$ slip are considered in order to model Ta) under planar flow conditions. The yield surface will be composed of the inner envelope of hyperplanes resulting from the yield facets of each individual slip system. For an incompressible material, the plane-strain yield surface will resemble a closed polygon, which can be expressed as a single curve on the $(\sigma_{11} - \sigma_{22})/2, \sigma_{12}$ stress axes [30]. Such a configuration is shown in Figure 1.

Simo, Kennedy and Govindjee [27] give a geometric interpretation of this plasticity theory as providing a closest-point return algorithm to the yield surface. This being the case, we can observe that the plastic straining will be coaxial with the trial elastic stress *only* when the trial stress is perpendicular to a particular yield facet. For example, when $\sigma_{11}^{tr} = -\sigma_{22}^{tr} > \frac{1}{2}\tau^\alpha$, the final stress state will be on the $(1\bar{1}0)$ $[11\bar{1}]$ facet at the $(\sigma_{11} - \sigma_{22})/2$ axis. When this is not the case (for example, when $\sigma^{tr} = \sigma_1^{tr}$, as shown in Figure 1) the resulting stress state, σ_1 , will not be coaxial with the straining increment, and after successive straining increments, the resulting stress state will migrate toward a vertex in the yield surface. Once the trial state falls within a zone in stress space bounded by normals to more than one yield facet (for example, σ_2^{tr}) multiple yield facets will be active, and the resulting stress state will remain at the vertex, σ_2 , until a change in strain path is significant enough to move the response away from the vertex.

Since the current hyperplane representation of each facet does not actually incorporate any explicit description of the yield vertex, it is possible for the algorithm to occasionally “mistake” some single-facet stress states (trial stress states that should only excite one yield facet) for vertex stress states. Figure 2 shows two hyperplanes from Figure 1; it is, essentially, an exploded view of Figure 1. The trial stress state depicted in this figure can easily be seen to violate both yield facets shown. Of all the possible stress states along the yield surface, it is actually σ_3 , and not the vertex, that minimizes plastic work (closest point projection). It is necessary, therefore, to check the vertex solution given by this algorithm against a normal return to each yield facet and accept the solution that minimizes the plastic work. At this point in the algorithm, the solution is also checked for numerical accuracy in order to ensure that

$$\sum_{\alpha}^{M_{act}} |f^\alpha| \leq tol, \quad (31)$$

where $tol = \tau_c \times 10^{-4}$. If this condition is violated, then the single facet solution that minimizes the plastic work is accepted as the final stress state.

3.2 Length-Scale Interaction

The modified Taylor polycrystal averaging scheme (Asaro and Needleman [6]) is incorporated in order to (1) interact the macroscopic deformation with the local grains, and (2) average the resulting stresses from the local grains to the associated aggregate stresses. The model assumes that deformation within a grain is uniform and that each grain under-

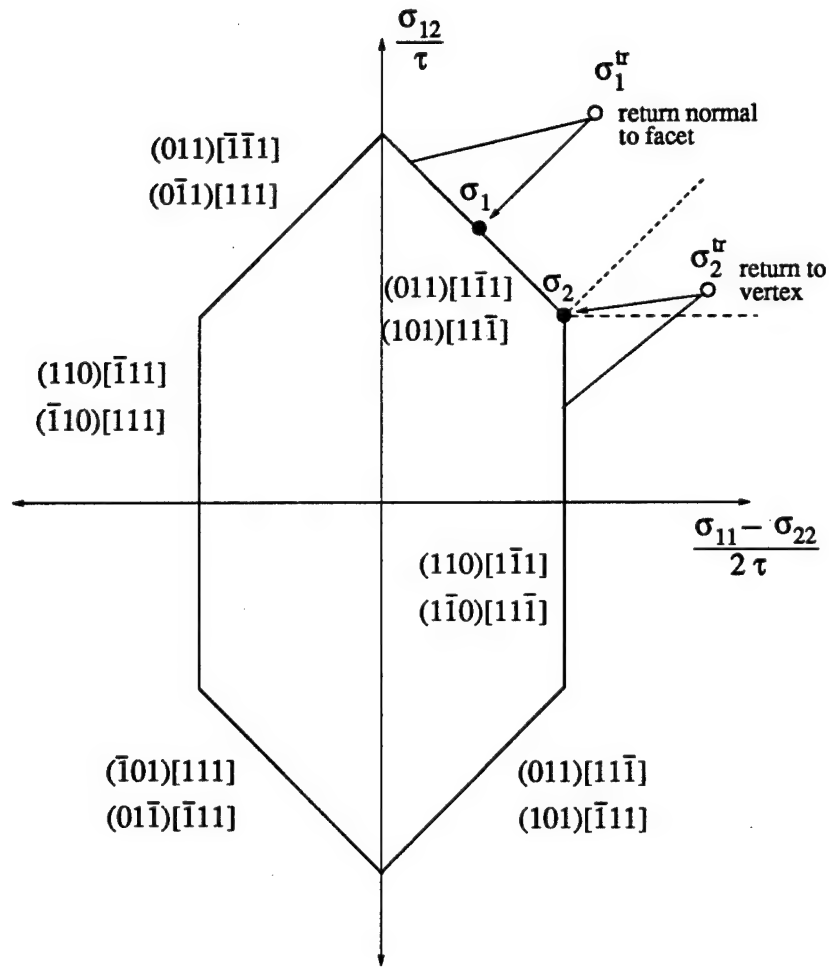


Figure 1. Six facets composing the 2D plane strain yield surface for the $\{110\}$ $\langle 111 \rangle$ slip family in a single crystal aligned with the macroscopic axes of stress

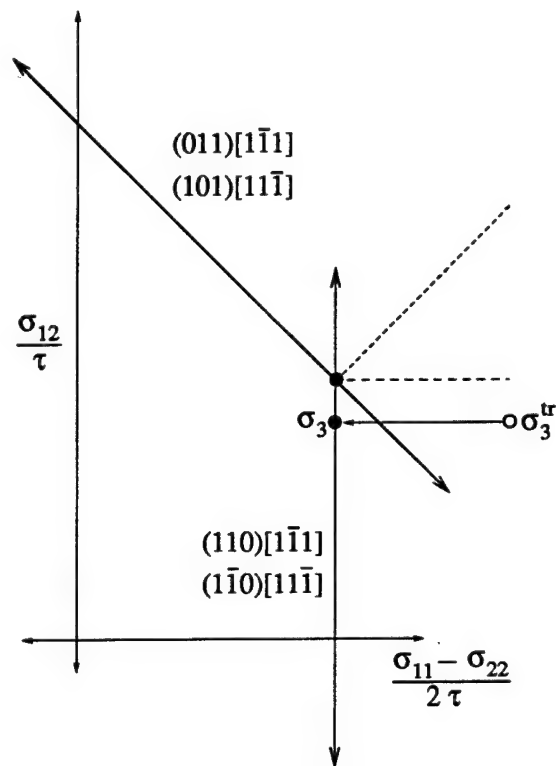


Figure 2. Enlarged view of two yield facets from Figure 1 showing an anomaly in the algorithm and the correct returned position

goes the same deformation as the entire aggregate. Therefore, the local velocity gradient, \mathbf{L} , is identical to the macroscopic velocity gradient, $\bar{\mathbf{L}}$. In this way, deformation compatibility between the grains and macroscopic deformation is maintained. After rotating the applied $\bar{\mathbf{L}}$ to \mathbf{L} , i.e.,

$$\mathbf{L}^g = (\boldsymbol{\Phi}^{(g)})^T \cdot \bar{\mathbf{L}} \cdot \boldsymbol{\Phi}^{(g)}, \quad (32)$$

the local Cauchy stresses, $\boldsymbol{\sigma}$, are then calculated and volume averaged to achieve the macroscopic stress, $\bar{\boldsymbol{\sigma}}$. Since the calculations assume that all the grains occupy an equal volume within the polycrystal,

$$\bar{\boldsymbol{\sigma}} = \frac{1}{K} \sum_{g=1}^K \boldsymbol{\Phi}^{(g)} \cdot \boldsymbol{\sigma}^{(g)} \cdot (\boldsymbol{\Phi}^{(g)})^T, \quad (33)$$

where K is the number of grains in the aggregate.

4. Application to Dynamic Deformation in Pure Ta

The purpose of this section is to show how the previously described model can be incorporated to resolve problems in dynamic, nonhomogeneous texture evolution; Increasingly complex examples of high-rate texture evolution in pure Ta are discussed. In this section, Ta, a body-centered-cubic (bcc) lattice structure material, was taken to deform by restricted glide on a total of 24 $\{110\}\langle 111 \rangle$ and $\{112\}\langle 111 \rangle$ slip systems. Both the slip resistance and the evolution of slip resistance on each system are taken as equal (i.e., Taylor hardening), and the material constants used in describing the resistance to slip on each slip system were obtained from the data reported in Chen and Gray [16] and scaled by a polycrystal Taylor factor of 3.58, as reported by Maudlin et al. [5] for the same Ta plate stock.

4.1 Uniaxial Compression

The first example is to model homogeneous uniaxial compression of a Ta cylinder. In this example, a single finite-element was compressed under uniaxial strain at a constant rate of 10^3 s^{-1} to a final true strain of 1.0. The element initially consisted of 300 random-oriented grains; after a true strain of 1.0, the resulting texture is shown in Figure 3. This result is consistent with high-rate texture data obtained by Lee et al. [9] and generally consistent with textures obtained in bcc materials (Schoenfeld et al. [8]; Kad and Schoenfeld [29]).

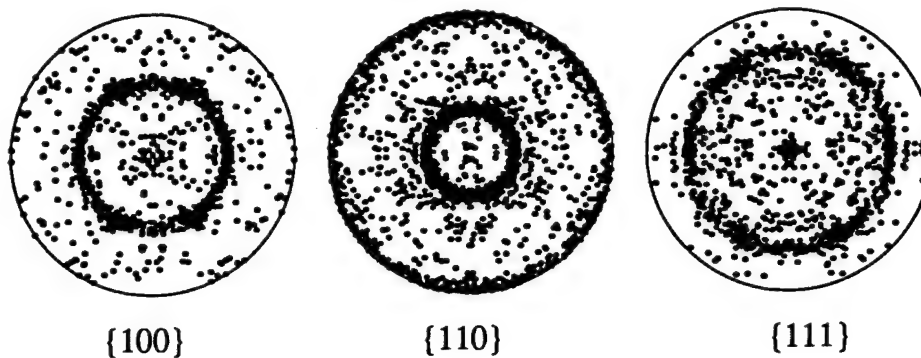


Figure 3. $\{100\}$, $\{110\}$, and $\{111\}$ pole figures for Ta compressed uniaxially to a true strain of 1.0

4.2 Taylor Impact Cylinder

Maudlin et al. [4] removed Ta cylinder specimens from “heavily” rolled Ta plate. The length-to-diameter ratio (L/D) of the specimens was 5, and they were removed such that the cylinder axis was parallel to the confined (i.e., transverse) direction of the rolled plate. The authors then launched the specimens from a .30-cal. Mann powder gun at a velocity of 175 m/s into target 4340 steel.

In order to model the previously mentioned experiment, a finite element model similar to that used by the authors was constructed using the EPIC96 computer code and implemented with the current model. A total of 12,960 tetrahedral elements were arranged in an $L/D = 5$ cylinder and impacted into a frictionless surface. It is known that the original plate was “heavily” rolled, so an assumed initial texture corresponding to plane strain compression was imparted to 48 grains at the gauss point of each element. This initial texture is shown at time = 0 in Figure 4, which contains $\{100\}$, $\{110\}$, and $\{111\}$ pole figures from the center of the impacted surface before, during, and after the forming event. From the figure, texture evolution from the initially rolled material to that characteristic of uniaxial compression (Figure 3) can be observed. Note that by 5 μ s, the initial texture has almost completely disappeared and that the strong components of the uniaxial texture do not begin to form until about 50 μ s. In spite of this rapid evolution toward an axisymmetric texture at the impacted surface, material away from the impacted surface undergoes a much less drastic evolution and thus, retains a great deal of the initial anisotropy.

Figure 5(a) shows contours of effective plastic strain in the ovalized footprint on the impact surface. Even though the texture at the center of the footprint evolves in an axisym-

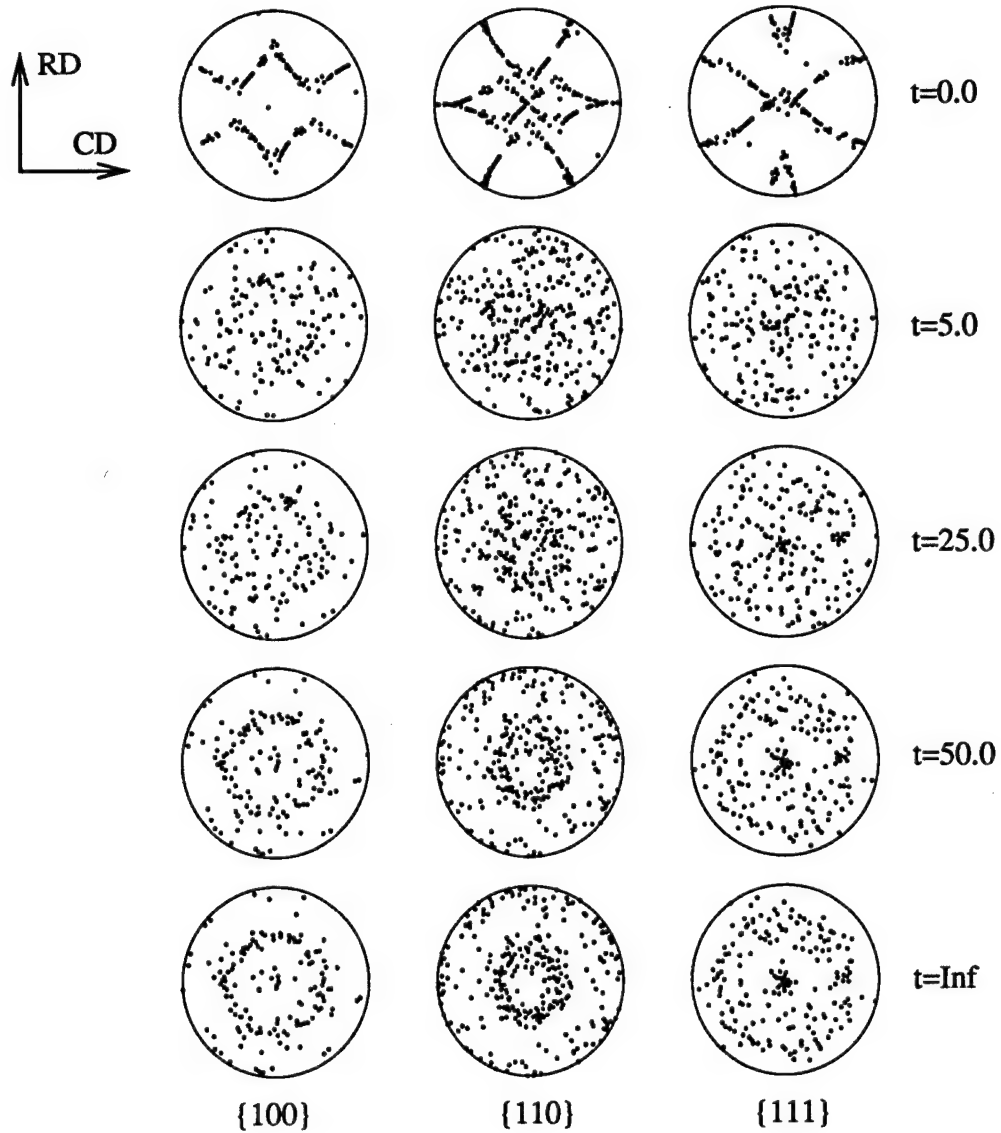


Figure 4. Evolution history of the $\{100\}$, $\{110\}$, and $\{111\}$ pole figures at the center of the impacted surface during the Taylor-cylinder impact experiment. Pole figures are shown along the impact direction; this direction was previously the transverse direction in the rolled Ta sheet material

metric manner, the material behind (away from the impacted surface) retains an amount of anisotropy from the initial conditions. Thus, the initially circular surface becomes “ovalized.” Figure 5(b) shows a view of the cylinder from the surface away from the impact site. The circular top of the cylinder is shown as a reference to the ovalized footprint at the impact site. Maudlin et al. [4] reported the ratio of the major axis to the minor axis of the elliptical foot to be 1.17. Using their anisotropic plasticity model to reflect the initial material anisotropy, the authors predict this ratio to be 1.15, by accounting for the evolution of texture, the current calculation predicts the ratio as 1.18.

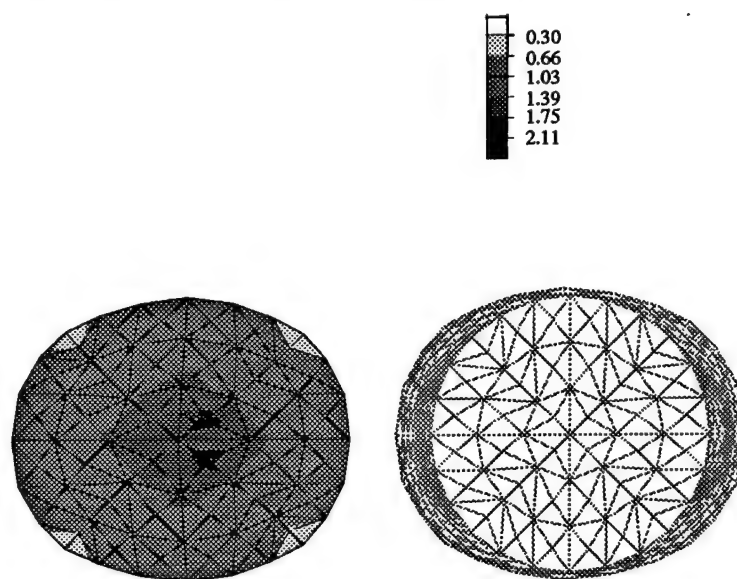


Figure 5. Two views along the impact direction of the Taylor cylinder; (a) contours of effective plastic strain in the ovalized footprint, and (b) the ovalized footprint relative to the initially circular cross section which is retained away from the impact surface

In this case, it is the initial anisotropy of the material away from the impacted surface that adds asymmetric confinement to deformation in the foot. Thus, from a structural analysis point of view, the texture evolution, although extreme on the impact surface, is not a major contributor to the ovaled footprint.

4.3 Explosive Deep-Drawing

In this section, the explosive deep-drawing of a cup-like shape from an initially flat disk is discussed. This is a highly simplified version of many other explosive-forming geometries, yet relevant in that we can examine through-thickness thinning, and thus the onset of both

diffuse and localized failure modes as a function of the initial arrangement of Ta single crystals within the macroscale aggregate.

Initially, a thin (relative to the specimen radius) disk of pure Ta is simply set on top of a high-explosive cylinder. The explosive is initiated on the cylinder face opposite the Ta disk, and the resulting transmitted shock imparts both a macroscopic acceleration to the disk and deformation into a cup-like configuration. To enhance the deep-drawability of the final cup shape, it is highly desirable for the workpiece to be resistant to through-thickness thinning. The initial geometry is represented in the bottom of Figure 6 by an axisymmetric finite element mesh. The Ta disk is represented by 240 symmetric crossed-triangular elements with 12 elements through the thickness. The initial grain distribution, shown in Figure 7, is assumed to be random and homogeneously distributed throughout the disk. At 50 μ s after initiation of the high explosive, the original disk shape is deformed into a cup with an upward velocity of approximately 760 m/s. Contours of effective plastic strain (top portion of Figure 6) show that high strain regions after deformation are both in the nose and tail regions of the deformed cup.

After deformation, individual grains within the Ta microstructure begin to accumulate around certain preferred orientations (i.e., we begin to develop texture). As the texture evolves, it also becomes graded along the radial direction. The center row of Figure 7 shows the evolved texture in the nose region where a strong $\{111\}$ fiber texture has developed due to the predominant uniaxial-compression deformation in this region. This is consistent with our previous result and also with those of Lee et al. [9], who show that Ta under uniaxial compression evolves both a strong $\{111\}$ fiber texture and a weak $\{100\}$ fiber texture. In the current calculation, it is the small number of grains that prevents us from picking up the weak $\{100\}$ component. Note, however, that 5 grains out of 48 are present within 10° of the center in the $\{100\}$ pole figure. Also note that stress calculations take place at the element centroid, off the axis of symmetry, and thus deviate from ideal, uniaxial compression.

The bottom row of Figure 7 is taken from the high-strain tail region depicted in Figure 6. In these pole figures, we see the presence of a strong $\{111\}$ fiber and a weaker $\{100\}$ texture except that both are rotated away from the the projectile axis due to large shear strains that develop in this region.

The previous example is illustrative of the kind of texture evolution that can be expected in Ta during explosive loading. Of more direct importance, however, are the effects of initial

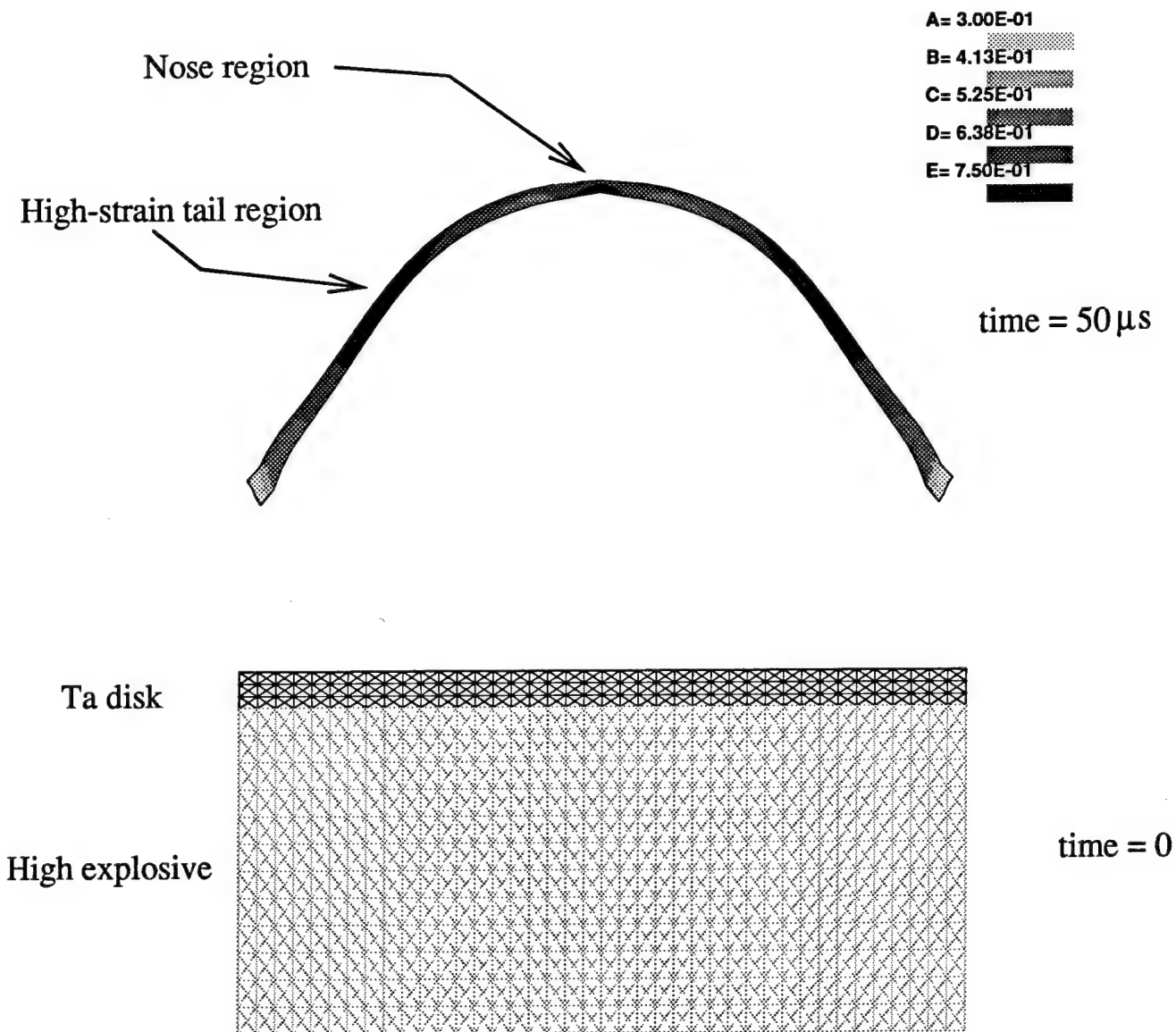


Figure 6. The explosive deep-drawing process; an initial finite element mesh (bottom) depicting a Ta disk and high-explosive charge. Initiation of the explosive imparts both an upward velocity to the disk and deformation into a cup-like configuration. Effective strain contours in the explosively deep-drawn disk at $50 \mu s$ are shown at the top of the figure

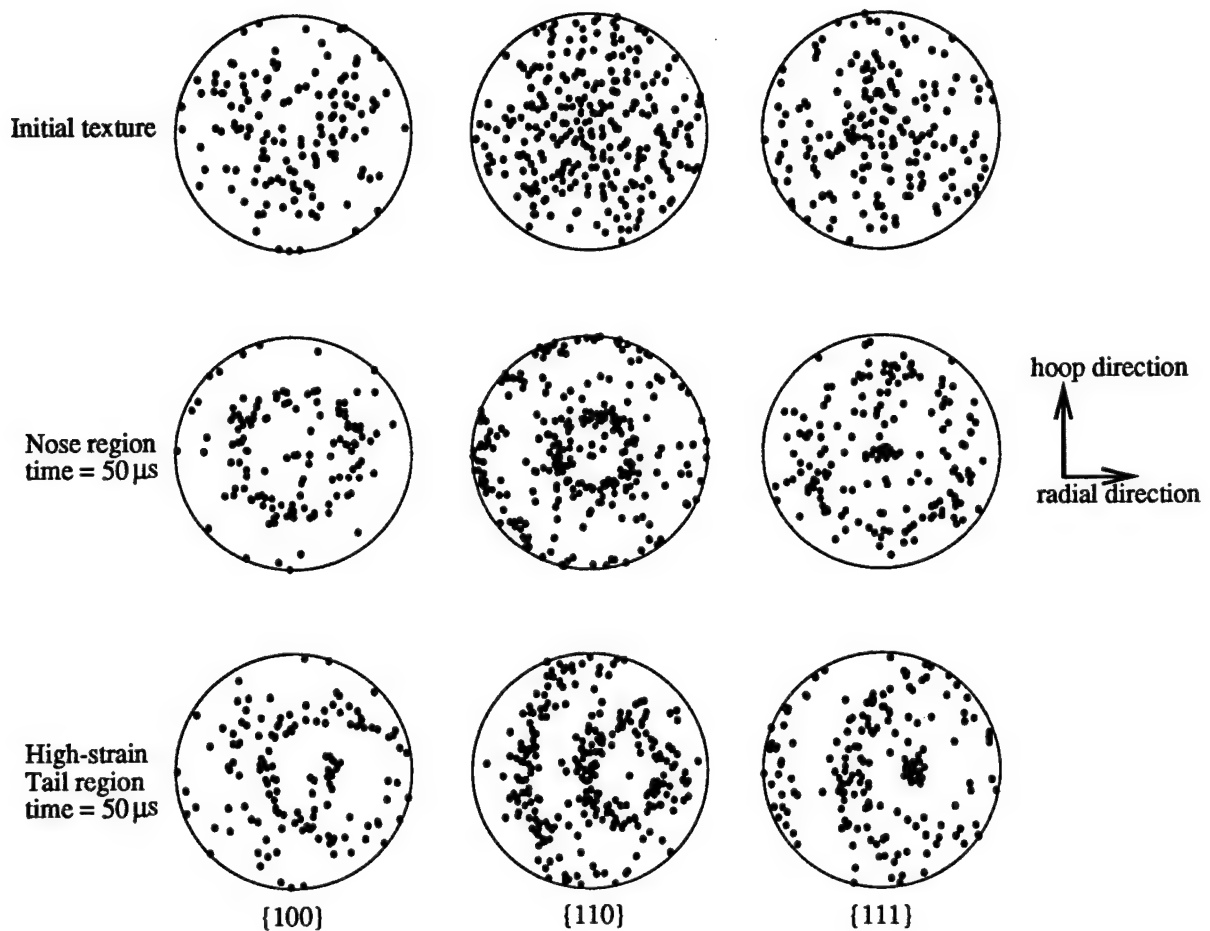


Figure 7. Texture evolution during explosive deep-drawing. Columns show the $\{100\}$, $\{110\}$, and $\{111\}$ pole figures. The top row characterizes the initially random distribution of grains that is homogeneous throughout the disk. By $50 \mu s$, there is a gradient in texture from the nose (center row) extending radially outward in the deep-drawn cup. Texture in the high-strain tail region is shown in the bottom row

orientations, and thus material anisotropy, in mitigating material failure during this kind of forming. In a series of articles, Clark et al. [31, 32, 33] examine the effects of thermomechanical processing variables on the production of Ta sheet products. Based on observations that bcc steels [34] with a strong $\{111\}$ fiber orientation have enhanced deformation characteristics during mechanical deep-drawing, the authors examined combinations of upset forging and cross rolling, as well as various heat treatments, with the aim of producing a strong $\{111\}$ fiber-oriented Ta sheet. The authors examined only processing variables on the sheet product; they did not discuss the deep-drawability of these products. They were, however, able to show that different dominant peaks in the orientation distribution function (ODF) for the sheet could be tailored by varying the processing schedule.

Following the work of these authors, it is desirable to understand the effects of various initial textures on the explosive deep-drawing characteristics of Ta sheet. Perfect $\{100\}$, $\{110\}$, and $\{111\}$ fiber textures were produced by aligning a grain with its $\{100\}$, $\{110\}$, or $\{111\}$ plane, respectively, normal to the plane of the sheet. Random rotations within that plane produced the initial distributions of 48 grains shown in the first column of Figure 8. These initial fiber textures were incorporated into the previous analysis. It is felt that by understanding how each individual texture component manifests itself in terms of macroscopic flow and resistance to thinning, we can gain a better understanding of the optimal microstructure for this application.

The second column in Figure 8 shows how the initially ideal fiber textures evolve in the apex of the explosively formed cup. Both the $\{100\}$ and the $\{111\}$ fibers remain intact throughout the deformation. Since the predominant deformation in this region is uniaxial compression, this is in direct agreement with Lee et al. [9] who observe that both $\{111\}$ and $\{100\}$ fiber textures are stable under uniaxial compression. Lee et al. [9] also observe that $\{110\}$ fiber orientations evolve into $\{111\}$ fibers under uniaxial compression; this can be seen in Figure 8, where, at $50 \mu s$, the $\{110\}$ fiber in the nose region is shown to be in the process of evolving into a $\{111\}$ fiber. Grains originally oriented $\approx 33^\circ$ from the center of the pole figure are now moving toward the center. Further uniaxial deformation would complete the transition into an ideal $\{111\}$ fiber. In the tail region (last column of Figure 8), the effects of a higher shear-strain environment can be seen on the initial fiber textures.

Again, it is not really these textures or their final state per se that is macroscopically important, but their effects on the drawing process itself. Figure 9 shows that after only 3

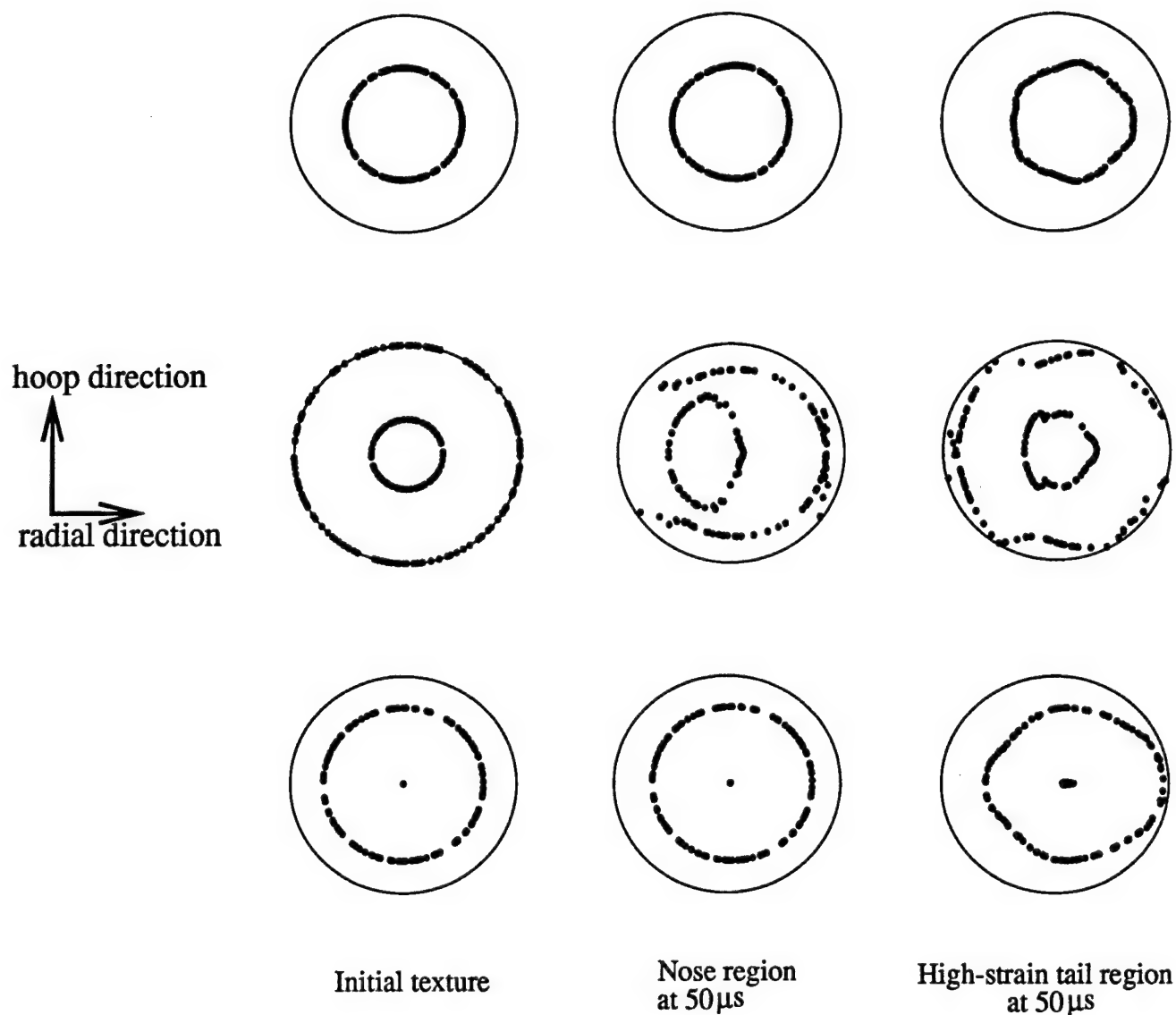


Figure 8. $\{111\}$ pole figures showing texture evolution due to three different ideal fiber textures. The initial homogeneous textures (first column) correspond to ideal $\{100\}$, $\{110\}$, and $\{111\}$ fiber textures. The second column shows final deformation textures in the nose region while the third column shows final texture in the high-strain tail region

μs into the calculation, the through-thickness stress levels in the $\{111\}$ and $\{110\}$ oriented disks are significantly higher than the disk with an initial $\{100\}$ fiber orientation. These stress levels directly reflect relative material anisotropy due to the different fiber textures and, consequently, the resistance to through-thickness thinning during the process.

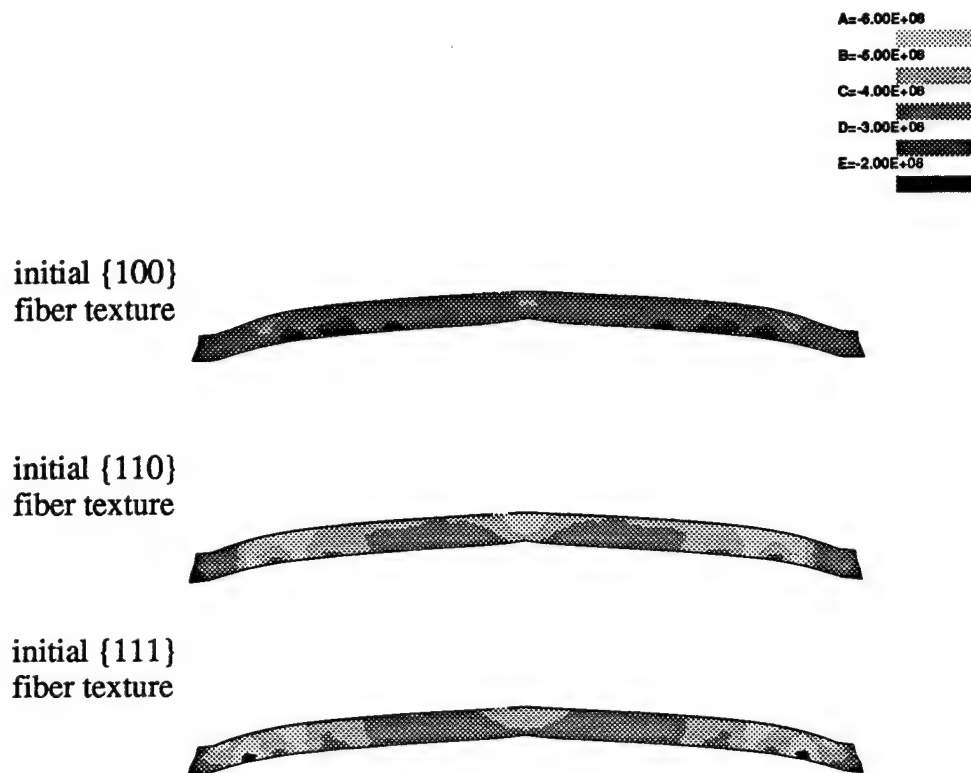


Figure 9. Contours of deviatoric through-thickness stress (units are in pascals) plotted on the deformed configuration of the explosively formed material at 3 μs

Figure 10 shows effective strain contours on the deformed shapes once formation is complete. By relative comparison, the workpiece with the initial $\{100\}$ fiber texture underwent much greater through-thickness deformations than either of the $\{110\}$ or the $\{111\}$ fiber-oriented workpieces. Specifically, large through-thickness thinning is apparent throughout the workpiece, with localizations occurring in both the nose and tail region. The $\{110\}$ and $\{111\}$ fibers produced approximately the same gross thinning through the cross section with the exception that the $\{110\}$ fiber produced a cup showing strong tendency for localization within the nose region, while the $\{111\}$ fiber gave only a slightly stronger diffuse necking region in the tail. It is also interesting to compare the forming result from the $\{111\}$ fiber-oriented material to that of the random-oriented material. Figure 11 reproduces these two calculations on opposing sides of the symmetric plane. It can be seen that the randomly

oriented material undergoes higher through-thickness strains; in particular, the nose region is approximately 30% thinner than the nose region in the $\{111\}$ fiber-oriented material. Overall, of the four calculations (three fiber textures and one randomly oriented material) the $\{111\}$ fiber seems to be the microscale arrangement of choice for explosive deep-drawing of bcc materials.

5. Discussion

The current article establishes a framework for modeling the high-strain-rate, nonhomogeneous evolution of anisotropy in polycrystalline Ta that is applicable to a broad class of ductile materials that deform primarily by bulk dislocation motion. Beginning with a rate- and temperature-dependent model for dislocations overcoming both intrinsic lattice resistance and barriers due to dislocation accumulation, the model focused on shear-stress/shear-strain behavior for slip systems in Ta single crystals. Incorporation of the restricted-glide kinematics and an appropriate numerical method for single crystals allowed for the resolution of individual crystal rotations, and thus the evolution of stress anisotropy, within the polycrystal.

Applications of the model were designed (1) to validate the model by way of connection to other work (since there is very little work on high-rate texture evolution and mechanical anisotropy in pure Ta, model validation is not a straightforward task); (2) to show that the model is capable of resolving nonhomogeneous evolution of texture; and, most importantly, (3) to illuminate anisotropic material behavior in Ta that is directly relevant to modern engineering applications.

For simple compression, it was shown that the current model depicted texture evolution consistent with Lee et al. [9]. The cylinder impact example was chosen to show that the model, while reflecting the expected texture evolution from a rolling-type texture to that which evolves under uniaxial compression, also exhibits macroscopic phenomena distinct to anisotropic materials (i.e., the ovalization of an initially circular footprint). The extent of ovalization was consistent with experimental work [4]. Finally, a detailed examination of an explosive-forming process revealed sensitivity of the final deformed shape to the initial microstructure. In particular, it was shown that an initial $\{111\}$ fiber texture resulted in a more stable through-thickness configuration than either the $\{100\}$ fiber texture or the

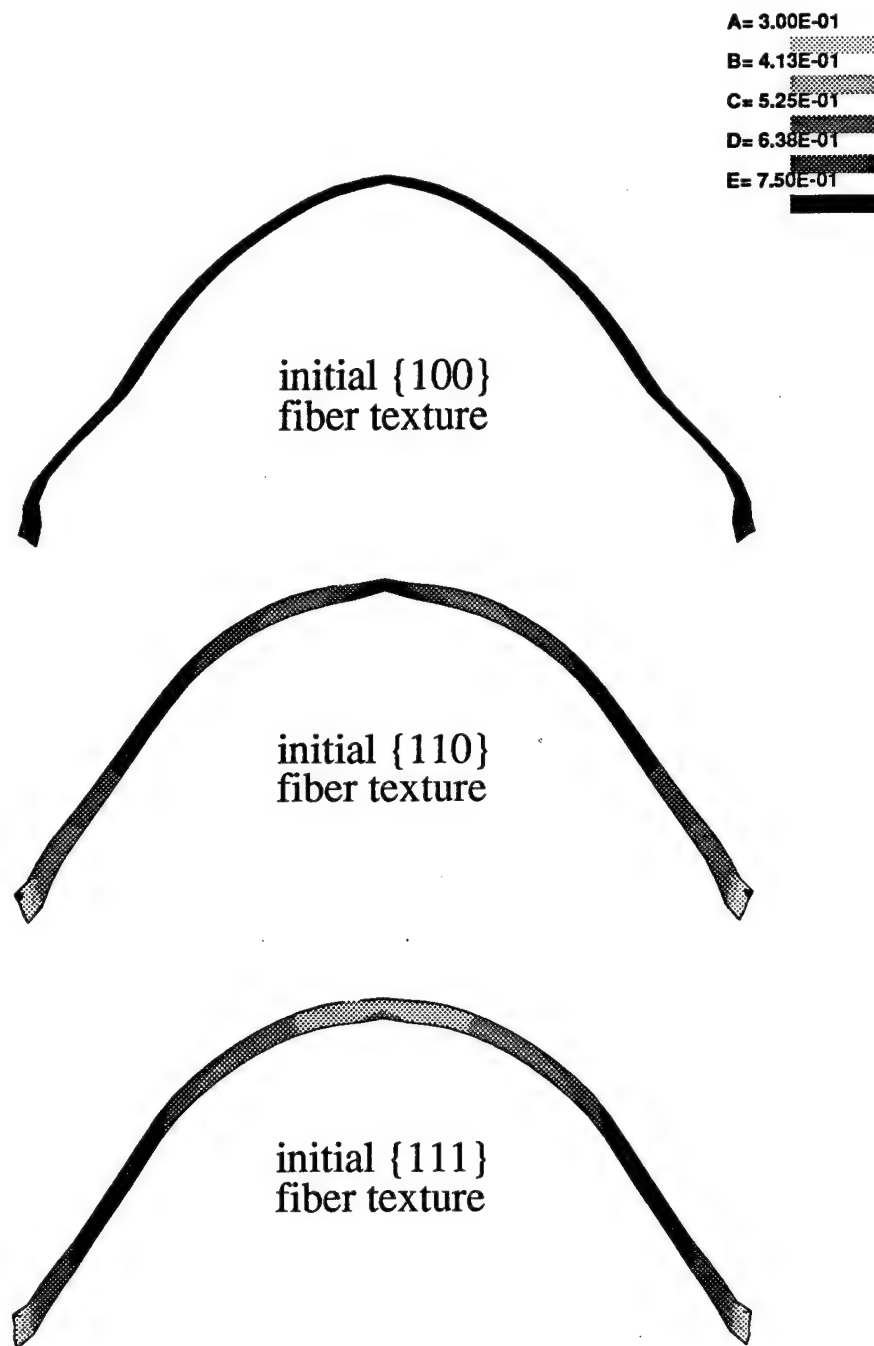


Figure 10. Effective strain contours on the deformed configuration for explosive deep-drawn material at 50 μ s. The initial textures were distributed homogeneously in the disk and then allowed to evolve with deformation.

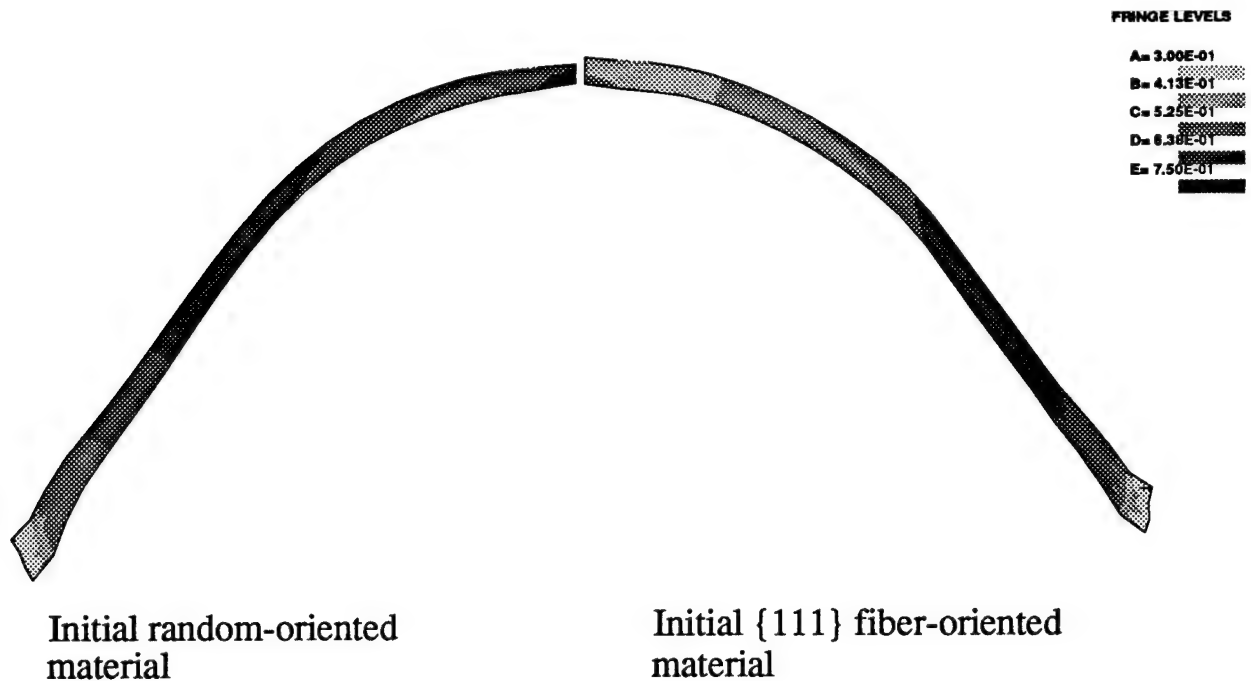


Figure 11. A comparison of effective strain contours over the deformed shapes from the initially random-oriented material and the material with an initial {111} fiber texture. The two calculations are shown on opposite sides of the plane of symmetry for the calculation

initially random microstructure. The relevance here is twofold. Clark et al. [31, 32, 33] showed that under common stock processing conditions, the extent of $\{111\} < uvw >$ versus $\{100\} < uvw >$ orientations is a *process-dependent* material property. Therefore, efforts to bias the initial material processing toward creating a strong and homogeneous $\{111\}$ fiber texture are not in vain. Further, since the initial $\{111\}$ fiber texture resulted in better flow properties than even the initial random-oriented material, current efforts to produce stock Ta via powder metallurgy methods may result in a suboptimal product.

6. References

1. Hill, R. "A Theory of the Yielding and Plastic Flow of Anisotropic Metals." *Proceedings of the Royal Society London*, vol. A193, p. 281, 1950.
2. Anderson, C. E., P. A. Cox, G. R. Johnson, and P. J. Maudlin. "A Constitutive Formulation for Anisotropic Materials Suitable for Wave Propagation Computer Programs." *Computational Mechanics*, vol. 15, p. 201, 1994.
3. Krieg, R. D., and S. W. Key. "Implementation of Time Dependent Plasticity Theory into Structural Computer Programs." *Constitutive Equations in Viscoplasticity: Computational and Engineering Aspects*, American Society of Mechanical Engineers, New

York, NY, p. 125, 1976.

4. Maudlin, P. J., S. I. Wright, G. T. Gray III, and J. W. House. "Application of Faceted Yield Surfaces for Simulating Compression Tests of Textured Materials." *Proceedings of the International Conference on Metallurgical and Materials Applications of Shock-Wave and High-Strain-Rate Phenomena*, El Paso, TX, August 1995.
5. Maudlin, P. J., S. I. Wright, U. F. Kocks, and M. S. Sahota. "An Application of Multi-surface Plasticity Theory: Yield Surfaces of Textured Materials." *Acta Materialia*, vol. 44, no. 10, p. 4027, 1996.
6. Asaro, R. J., and A. Needleman. "Texture Development and Strain Hardening in Rate Dependent Polycrystals." *Acta Metallurgica et materialia*, vol. 33, p. 923, 1985.
7. Nemat-Nasser, S. and M. Obata. "Rate-dependent, Finite Elasto-Plastic Deformation of Polycrystals." *Proceedings of the Royal Society of London*, vol. A407, p. 343, 1986.
8. Schoenfeld, S. E., S. Ahzi, and K. S. Vecchio. "Modeling Dynamic Behavior and Texture Evolution in Pure Ta." *Tantalum*, edited by E. Chen, A. Crowson, E. Lavernia, W. Ebihara, and P. Kumar, TMS publications, 1996.
9. Lee, B. J., K. S. Vecchio, S. Ahzi, and S. E. Schoenfeld. "Modeling Mechanical Behavior of Tantalum." *Metallurgical and Materials Transactions A.*, vol. 28A, p. 113, 1997.
10. Kalidindi, S. R., C. A. Bronkhorst, and L. Anand. "Crystallographic Texture Evolution in Bulk Deformation Processing of Fcc Metals." *Journal of Mechanics and Physics of Solids*, vol. 40, p. 537, 1992.
11. Beaudoin, A. J., K. K. Mathur, P. R. Dawson, and G. C. Johnson. "Process Simulation With Explicit Use of Polycrystalline Plasticity Models." *International Journal of Plasticity*, vol. 9, p. 833, 1993.
12. Kothari, M., and Anand, L. "Elasto-Viscoplastic Constitutive Equations for Polycrystalline Metals: Application to Tantalum." *Submitted to International Journal of Plasticity*, 1997.
13. ABAQUS Reference Manuals, Hibbit, Karlson, and Sorensen Inc., Pawtucket, RI, 1995.
14. Kocks, U. F., A. S. Argon, and M. F. Ashby. "Thermodynamics and Kinetics of Slip." *Progress in Material Science*, vol. 19, Pergamon Press, London, 1975.
15. Follansbee, P. S. and G. T. Gray III. "An analysis of the Low Temperature, Low and High Strain-Rate Deformation of Ti-6Al-4V." *Metallurgical and Materials Transactions A.*, vol. 20A, p. 863, 1989.
16. Chen, S. R., and G. T. Gray III. "Constitutive Behavior of Tantalum and Tantalum-Tungsten Alloys." *Metallurgical and Materials Transactions A.*, vol. 27A, 1996.
17. Christian, J. W. *Metallurgical and Materials Transactions A.*, vol. 14, p. 1237, 1983.
18. Hoge, K. G. and A. K. Mukherjee. "The Temperature and Strain Rate Dependence of Flow Stress in Tantalum." *Journal of Material Science*, vol. 12, p. 1666, 1977.
19. Mecking, H., and U. F. Kocks. "Kinetics of Flow and Strain-Hardening." *Acta Metallurgica et materialia*, vol. 29, p. 1865, 1981.
20. Peirce, D., R. J. Asaro, and A. Needleman. "Material Rate Dependence and Localized Deformation in Crystalline Solids." *Acta Metallurgica et materialia*, vol. 31, p. 1951, 1983.

21. Lee, E. H. "Elastic-Plastic Deformation at Finite Strains." *Journal of Applied Mechanics*, vol. 36, p. 1, 1969.
22. Rice, J. R. "Inelastic Constitutive Relations for Solids: An Internal-Variable Theory and its Application to Metal Plasticity." *Journal of the Mechanics and Physics of Solids*, vol. 19, p. 433, 1971.
23. Hill, R. and K. S. Havner. "Perspectives in the Mechanics of Elastoplastic Crystals." *Journal of the Mechanics and Physics of Solids*, vol. 30, p. 5, 1982.
24. Asaro, R. J., "Crystal Plasticity." *Journal of Applied Mechanics*, vol. 5, p. 921, 1983.
25. Johnson, G. R., R. A. Stryk, T. J. Holmquist, and S. R. Beissel. "Numerical Algorithms in the EPIC Code, Preliminary Report." Alliant Techsystems Inc., Hopkins, MN, 1996.
26. Koiter, W. T. "Stress-Strain Relations, Uniqueness and Variational Theorems for Elastic-Plastic Materials with a Singular Yield Surface." *Quarterly of Applied Mathematics*, vol. 11, p. 350, 1953.
27. Simo, J. C., J. G. Kennedy, and S. Govindjee. "Non-Smooth Multisurface Plasticity and Viscoplasticity. Loading/Unloading Conditions and Numerical Algorithms." *International Journal of Numerical Methods in Engineering*, vol. 26, p. 2161, 1988.
28. Asaro, R. J. and J. R. Rice. "Strain Localization in Ductile Single Crystals." *Journal of Mechanics and Physics of Solids*, vol. 25, p. 309, 1977.
29. Kad B. K., S. E. Schoenfeld, R. J. Asaro, C. J. McKamey. "Deformation Textures in Fe3Al Alloys: An Assessment of Dominant Slip System Activity in the 900-1325 K Temperature Range of Hot Working." *Acta Metallurgica et materialia*, vol. 45, 1997.
30. Rice, J. R. *Journal of Mechanics and Physics of Solids*, vol. 21, p. 63, 1973.
31. Clark, J. B., R. K. Garrett Jr., T. J. Jungling, R. A. Vandermeer. and C. L. Vold. "Effect of Processing Variables on Texture and Texture Gradients in Tantalum." *Metallurgical and Materials Transactions A*, vol. 22, p. 2039, 1991.
32. Clark, J. B., R. K. Garrett Jr., T. J. Jungling,, and R. I. Asfahani. "Influence of Initial Ingot Breakdown on the Microstructural and Textural Development of High-Purity Tantalum." *Metallurgical and Materials Transactions A*, vol. 22, p. 2959, 1991.
33. Clark, J. B., R. K. Garrett Jr., T. J. Jungling, and R. I. Asfahani. "Influence of Transverse Rolling on the Microstructural and Texture Development in Pure Tantalum." *Metallurgical and Materials Transactions A*, vol. 22, p. 2039, 1991.
34. Lankford, W. T., S. C. Snyder, and J. C. Bauscher. "New Criteria for Predicting the Press Performance of Deep Drawing Sheets." *Transactions of the American Society of Metals*, vol. 42, p. 1197, 1950.

INTENTIONALLY LEFT BLANK

| <u>NO. OF</u> <u>COPIES</u> | <u>ORGANIZATION</u> | <u>NO. OF</u> <u>COPIES</u> | <u>ORGANIZATION</u> |
|--------------------------------|--|--------------------------------|---|
| 2 | DEFENSE TECHNICAL INFORMATION CENTER DTIC DDA 8725 JOHN J KINGMAN RD STE 0944 FT BELVOIR VA 22060-6218 | 1 | DPTY ASSIST SCY FOR R&T SARD TT T KILLION THE PENTAGON WASHINGTON DC 20310-0103 |
| 1 | HQDA DAMO FDQ DENNIS SCHMIDT 400 ARMY PENTAGON WASHINGTON DC 20310-0460 | 1 | OSD OUSD(A&T)/ODDDR&E(R) J LUPO THE PENTAGON WASHINGTON DC 20301-7100 |
| 1 | CECOM SP & TRRSTR L COMMCTN DIV AMSEL RD ST MC M H SOICHER FT MONMOUTH NJ 07703-5203 | 1 | INST FOR ADVNCD TCHNLGY THE UNIV OF TEXAS AT AUSTIN PO BOX 202797 AUSTIN TX 78720-2797 |
| 1 | PRIN DPTY FOR TCHNLGY HQ US ARMY MATCOM AMCDCG T M FISETTE 5001 EISENHOWER AVE ALEXANDRIA VA 22333-0001 | 1 | DUSD SPACE 1E765 J G MCNEFF 3900 DEFENSE PENTAGON WASHINGTON DC 20301-3900 |
| 1 | PRIN DPTY FOR ACQUSTN HQS US ARMY MATCOM AMCDCG A D ADAMS 5001 EISENHOWER AVE ALEXANDRIA VA 22333-0001 | 1 | USAASA MOAS AI W PARRON 9325 GUNSTON RD STE N319 FT BELVOIR VA 22060-5582 |
| 1 | DPTY CG FOR RDE HQS US ARMY MATCOM AMCRD BG BEAUCHAMP 5001 EISENHOWER AVE ALEXANDRIA VA 22333-0001 | 1 | CECOM PM GPS COL S YOUNG FT MONMOUTH NJ 07703 |
| | | 1 | GPS JOINT PROG OFC DIR COL J CLAY 2435 VELA WAY STE 1613 LOS ANGELES AFB CA 90245-5500 |
| | | 1 | ELECTRONIC SYS DIV DIR CECOM RDEC J NIEMELA FT MONMOUTH NJ 07703 |

| <u>NO. OF</u> <u>COPIES</u> | <u>ORGANIZATION</u> | <u>NO. OF</u> <u>COPIES</u> | <u>ORGANIZATION</u> |
|--------------------------------|---|--------------------------------|---|
| 3 | DARPA L STOTTS J PENNELLA B KASPAR 3701 N FAIRFAX DR ARLINGTON VA 22203-1714 | 3 | DIRECTOR US ARMY RESEARCH LAB AMSRL CI LL 2800 POWDER MILL RD ADELPHI MD 20783-1145 |
| 1 | SPCL ASST TO WING CMNDR 50SW/CCX CAPT P H BERNSTEIN 300 O'MALLEY AVE STE 20 FALCON AFB CO 80912-3020 | 3 | DIR USARL AMSRL CI LP (305) |
| 1 | USAF SMC/CED DMA/JPO M ISON 2435 VELA WAY STE 1613 LOS ANGELES AFB CA 90245-5500 | 2 | DIRECTOR LLNL L-170 D LASSILA L-355 A SCHWARTZ |
| 1 | US MILITARY ACADEMY MATH SCI CTR OF EXCELLENCE DEPT OF MATHEMATICAL SCI MDN A MAJ DON ENGEN THAYER HALL WEST POINT NY 10996-1786 | 1 | NAVAL SURFACE WARFARE CENTER INDIAN HEAD DIVISION ATTN: R.K. GARRETT, JR. BLDG 841 ROOM 20 101 STRAUSS AVE INDIAN HEAD, MD 20640 |
| 1 | DIRECTOR US ARMY RESEARCH LAB AMSRL CS AL TP 2800 POWDER MILL RD ADELPHI MD 20783-1145 | 1 | NAVAL SURFACE WARFARE CENTER CARDEROCK DIVISION ATTN: JOHN MCKIRGAN 9500 MACARTHUR BLVD WEST BETHESDA MD 20817-5700 |
| 1 | DIRECTOR US ARMY RESEARCH LAB AMSRL CS AL TA 2800 POWDER MILL RD ADELPHI MD 20783-1145 | 1 | COMMANDER US ARMY ARDEC ATTN: AMSTA AR FSA E E BAKER PICATINNY ARSENAL NJ 07806-5000 |

NO. OF
COPIES

ORGANIZATION

NO. OF
COPIES

ORGANIZATION

68

DIR USARL
AMSRL WM T, W MORRISON
AMSRL WM TD
A DIETRICH
T FARRAND
K FRANK
S SCHOENFELD (10 CP)
A GUPTA
M RAFTENBERG
M SCHEIDLER
S SEGLETES
J WALTER
T WRIGHT
S SCHOENFELD
AMSRL WM TA
S BILYK
W BRUCHEY
G BULMASH
M BURKINS
J DEHN
G FILBEY
W GILLICH
W GOOCH
D HACKBARTH
T HAVEL
E HORWATH
Y HUANG
H MEYER
E RAPACKI
J RUNYEON
N RUPERT
M ZOLTOSKI
AMSRL WM WD, A NILER
AMSRL WM MD, R DOWDING

AMSRL WM TC
W DEROSSET
K KIMSEY
M LAMPSON
L MAGNESS
D SCHEFFLER
G SILSBY
R SUMMERS
W WALTERS
AMSRL WM MF
S CHOU
D DANDEKAR
R RAJENDRAN
T WEERASOORIYA
D GROVE
AMSRL WM M
D VIECHNICKI
J MCCAULY
G HAGNAUER
AMSRL WM ME
M WELLS
R ADLER
M STAKER
AMSRL WM MC
M CHEN
G GILDE
P HAUNG
T HYNES
J SWAB
J WELLS
J CASALVIA
C HUBBARD
M COLE

INTENTIONALLY LEFT BLANK

| REPORT DOCUMENTATION PAGE | | | Form Approved OMB No. 0704-0188 | |
|--|---|--|--|--|
| <small>Public reporting burden for this collection of information is estimated to average 1 hour per response, including the time for reviewing instructions, searching existing data sources, gathering and maintaining the data needed, and completing and reviewing the collection of information. Send comments regarding this burden estimate or any other aspect of this collection of information, including suggestions for reducing this burden, to Washington Headquarters Services, Directorate for Information Operations and Reports, 1215 Jefferson Davis Highway, Suite 1204, Arlington, VA 22202-4302, and to the Office of Management and Budget, Paperwork Reduction Project (0704-0188), Washington, DC 20503.</small> | | | | |
| 1. AGENCY USE ONLY (Leave blank) | | 2. REPORT DATE December 1997 | 3. REPORT TYPE AND DATES COVERED Final, Jun 96 - Jun 97 | |
| 4. TITLE AND SUBTITLE Dynamic Behavior of Polycrystalline Tantalum | | | 5. FUNDING NUMBERS 61102AH43 | |
| 6. AUTHOR(S) Scott E. Schoenfeld | | | | |
| 7. PERFORMING ORGANIZATION NAME(S) AND ADDRESS(ES) U.S. Army Research Laboratory ATTN: AMSRL-WM-TD Aberdeen Proving Ground, MD 21005-5066 | | | 8. PERFORMING ORGANIZATION REPORT NUMBER ARL-TR-1560 | |
| 9. SPONSORING/MONITORING AGENCY NAMES(S) AND ADDRESS(ES) | | | 10. SPONSORING/MONITORING AGENCY REPORT NUMBER | |
| 11. SUPPLEMENTARY NOTES | | | | |
| 12a. DISTRIBUTION/AVAILABILITY STATEMENT Approved for public release; distribution is unlimited. | | | 12b. DISTRIBUTION CODE | |
| 13. ABSTRACT (Maximum 200 words) <p>A description for the strain-rate and temperature-dependent behavior of pure tantalum (Ta) at large strains is developed. An integral part of the model incorporates the kinematics of crystallographic slip, and thus, the rotation of single crystals within the material, so as to reflect the evolution of anisotropy resulting from applied mechanical deformation. Such deformation is accommodated via bulk dislocation motion and governed by interactions that may or may not be thermally assisted. The model represents each discrete slip system as a single facet in a multisurface plasticity theory, which is well suited to high-rate numerical methods (explicit integration schemes). A formulation of this type allows for the complete kinematic decomposition of macroscopic material rotations and the rotations of single crystals due to motion through the lattice. Applications to high-rate deformation in polycrystals is conducted within a finite element implementation by invoking a Taylor criterion for interaction between the macroscopic and the mesoscopic (single-crystal) length scales. The model behavior is examined in application to high-rate problems with increasingly complex geometries (homogeneous uniaxial compression, the impact of a textured cylindrical bar into a rigid anvil, and the explosive deep-drawing of a Ta disk). The final example compares through-thickness deformation in the Ta disk as a function of initial texture and, therefore, emphasizes the profound effects of plastic anisotropy during finite deformation.</p> | | | | |
| 14. SUBJECT TERMS material modeling, anisotropy, explosive forming | | | 15. NUMBER OF PAGES 37 | |
| | | | 16. PRICE CODE | |
| 17. SECURITY CLASSIFICATION OF REPORT UNCLASSIFIED | 18. SECURITY CLASSIFICATION OF THIS PAGE UNCLASSIFIED | 19. SECURITY CLASSIFICATION OF ABSTRACT UNCLASSIFIED | 20. LIMITATION OF ABSTRACT UL | |

INTENTIONALLY LEFT BLANK.

USER EVALUATION SHEET/CHANGE OF ADDRESS

This Laboratory undertakes a continuing effort to improve the quality of the reports it publishes. Your comments/answers to the items/questions below will aid us in our efforts.

1. ARL Report Number/Author ARL-TR-1560 (Schoenfeld) Date of Report December 1997
2. Date Report Received _____
3. Does this report satisfy a need? (Comment on purpose, related project, or other area of interest for which the report will be used.) _____

4. Specifically, how is the report being used? (Information source, design data, procedure, source of ideas, etc.) _____

5. Has the information in this report led to any quantitative savings as far as man-hours or dollars saved, operating costs avoided, or efficiencies achieved, etc? If so, please elaborate. _____

6. General Comments. What do you think should be changed to improve future reports? (Indicate changes to organization, technical content, format, etc.) _____

CURRENT
ADDRESS

Organization

Name

E-mail Name

Street or P.O. Box No.

City, State, Zip Code

7. If indicating a Change of Address or Address Correction, please provide the Current or Correct address above and the Old or Incorrect address below.

OLD
ADDRESS

Organization

Name

Street or P.O. Box No.

City, State, Zip Code

(Remove this sheet, fold as indicated, tape closed, and mail.)
(DO NOT STAPLE)

DEPARTMENT OF THE ARMY

OFFICIAL BUSINESS

BUSINESS REPLY MAIL
FIRST CLASS PERMIT NO 0001,APG,MD

POSTAGE WILL BE PAID BY ADDRESSEE

DIRECTOR
US ARMY RESEARCH LABORATORY
ATTN AMSRL WM TD
ABERDEEN PROVING GROUND MD 21005-5066



NO POSTAGE
NECESSARY
IF MAILED
IN THE
UNITED STATES

